SPACE CHARGE EFFECT IN ISOCHRONOUS RINGS*

E. Pozdeyev, BNL, Upton, NY 11973, USA
J.A. Rodriguez, CERN, Geneva, Switzerland
F. Marti, R.C. York, NSCL, MSU, Lansing, MI 48824, USA

Abstract

Cyclotrons, rings for precise nuclear mass spectrometry, and some light sources with extremely short bunches are operated or planned to be operated in the isochronous or almost isochronous regime. Also, many hadron synchrotrons run in the isochronous regime for a short period of time during transition crossing. The longitudinal motion is frozen in the isochronous regime that leads to accumulation of the integral of the longitudinal space charge force. In low-gamma hadron machines, this can cause a fast growth of the beam energy spread even at modest beam intensities. Additionally, the transverse component of the space charge effectively modifies the dispersion function and the slip factor shifting the isochronous (transition) point. In this paper, we discuss space charge effects in the isochronous regime and present experimental results obtained in the Small Isochronous Ring, developed at Michigan State University specifically for studies of space charge in the isochronous regime.

INTRODUCTION

Numerical and experimental studies of space charge effects in the isochronous regime conducted at Michigan State University in 2001-2004 revealed that the space charge field could drive a fast longitudinal instability that caused breakup of coasting bunches in Small Isochronous Ring (SIR) within a few turns [1],[2]. In simulations, the instability was observed not only in the isochronous regime but also below the transition. Originally, the cause of this instability was not completely understood.

Significant efforts have been undertaken to understand the dynamics of intense beam at the transition energy in synchrotrons. Results of this studies have been documented elsewhere [3],[4]. Typically models used for these studies included the longitudinal component of the space charge force and its effect on the longitudinal motion. Transverse effects were limited to transverse defocusing due to the incoherent space charge field and the corresponding effective increase of the dispersion function (Umstätter effect [5]). However, none of these models seemed to be able to explain the beam behavior observed in SIR.

The observed instability can be explained by the effect of the radial component of the coherent space charge force on the coherent longitudinal motion. As shown later in this paper, this field can arise from deformation of the beam shape and cause a negative-mass-like instability even if the machine optics is set below the transition. The importance of including the transverse coherent field in the isochronous regime has been known for some time in the cyclotron community [6]; although, an analytical model of this process has not been developed.

* Work performed under the auspices of the U.S. Department of Energy and supported by the NSF Grant No. PHY 0110253

EFFECT OF COHERENT TRANSVERSE SPACE CHARGE FIELD

Longitudinal space charge impedance: short wavelength approximation

First, we demonstrate that the longitudinal impedance has a maximum at a wavelength comparable to the beam diameter. The resulting high frequency energy perturbation can cause a transverse offset of the beam centroid, which in turn can give rise to a transverse coherent electric field.

The space charge impedance per turn of a uniformly charged beam is given in the long wavelength limit by

$$Z_{||}(k) = ik\frac{Z_0 R_0}{\gamma^2\beta}\left(\frac{1}{2} - \ln\left(\frac{a}{b}\right)\right), \qquad (1)$$

where Z_0 is the characteristic vacuum impedance, 377 Ω, R_0 is the average radius an accelerator, γ and β are the relativistic factors, and a and b are the beam and the vacuum chamber radii respectively.

When the wavelength becomes comparable to the diameter of the vacuum chamber, equation (1) becomes invalid. In the short wavelength limit, the effect of image charges can be neglected and the impedance can be trivially obtained by direct integration of the electric field on the beam axis. For a round beam with a uniform transverse charge distribution, the longitudinal space charge impedance in the short wavelength limit is

$$Z_{||}(k) = i\frac{2Z_0 R_0}{ka^2\beta}\left(1 - \frac{ka}{\gamma}\cdot K_1\left(\frac{ka}{\gamma}\right)\right), \qquad (2)$$

where K_1 is the modified Bessel function of the second kind.

Figure 1 shows the longitudinal space charge impedance per turn in both long and short wavelength limits for a non-relativistic beam ($\gamma = 1$). The impedance reaches its absolute maximum at the wavelength approximately equal to 2.5 beam diameters.

Transverse space charge field

Perturbations of the longitudinal charge density produce a longitudinal electric field. Since the longitudinal motion is frozen in the isochronous regime, the effect of the longitudinal field accumulates with time, causing the correlated energy spread to grow. As the energy of particles changes,

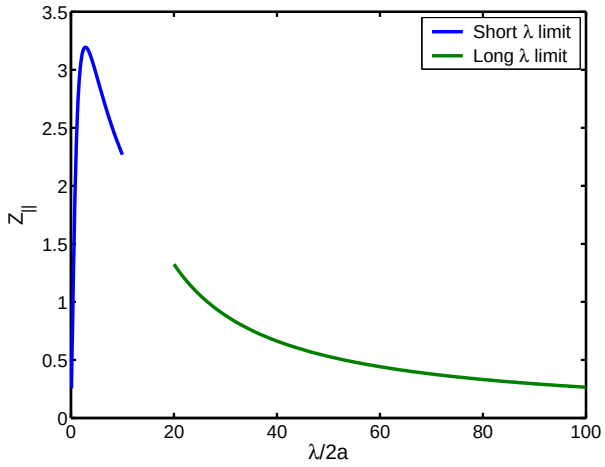

Figure 1: Longitudinal impedance (arb. units) in long and short wavelength approximations as a function of the wavelength normalized to the beam diameter, $2a$. The impedance reaches its maximum at $\lambda \approx 2.5$ beam diameter. The a/b ratio is equal to 5.

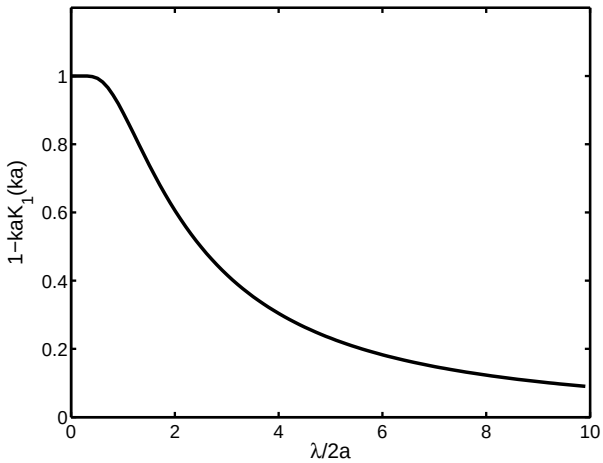

Figure 2: Factor $1 - ka \cdot K_1(ka))$ as a function of the wavelength normalized to the beam diameter, $2a$.

their transverse position also changes because of the radial dispersion. If the longitudinal charge density perturbation is a pure sinusoidal wave, the transverse displacement of the beam centroid is proportional to cosine with the same wavelength.

The radial wiggles of the beam centroid cause a transverse electric field. This field can result from two sources: a) image charges on the vacuum chamber that are responsible for the coherent tune shift and b) snaking itself. In this paper, we assume that the vacuum chamber is formed by two horizontal perfectly conducting planes and that the coherent radial field is only due to the beam snaking. Additionally, we will assume that initial perturbations of the linear charge density are small comparatively to the average charge density. Also, we will consider only the non-relativistic case ($\gamma = 1$). If the beam centroid displacement is proportional to cosine, the radial field on the beam centroid created by the beam wiggles has also a cosine dependence upon the longitudinal coordinate. If the beam wiggles are small comparatively to the beam radius, the coherent radial field at the beam centroid can be obtained by trivial integration, giving:

$$E_x = 2\pi\rho x_c(z)(1 - ka \cdot K_1(ka)), \tag{3}$$

where ρ is the charge density within the beam, $x_c(z)$ is the deviation of the beam centroid from the equilibrium orbit with no energy deviation. Figure 2 shows the factor $1 - ka \cdot K_1(ka))$ as a function of the wavelength. Note that the coherent transverse electric field due to the beam centroid wiggling is approximately equal to the incoherent space charge field within the beam, $2\pi\rho x$, for short wavelength perturbations and small x. In the long wavelength limit, the coherent field disappears.

Dispersion function and slip factor with space charge

The equation of radial motion can be approximately written in the smooth approximation and the low energy limit as

$$x'' + \frac{\nu^2}{R_0^2}x = \frac{1}{R_0}\frac{\delta p}{p} + \frac{eE_x}{m\beta^2 c^2}. \tag{4}$$

Using Eq. (3), one can easily find the steady state solution of this equation:

$$x_{ss} \approx \frac{R_0}{\nu^2}\left(1 + 2\left(\frac{-\delta\nu}{\nu}\right)_{sc}(1 - ka \cdot K_1(ka))\right)\frac{\delta p}{p} \tag{5}$$

where we expressed the charge density ρ via the incoherent space charge tune shift $(\delta\nu/\nu)_{sc}$, assuming uniform charge density. Thus, one can conclude that the coherent radial electric field caused by beam wiggling changes the dispersion function D by

$$\delta D \approx 2D\left(\frac{-\delta\nu}{\nu}\right)_{sc}(1 - ka \cdot K_1(ka)) \tag{6}$$

The dispersion function variation caused by the transverse component of the space charge force changes the slip factor. The modified slip factor is approximately given by

$$\begin{aligned}\eta_s &= \eta_{s0} + \frac{\delta D}{R_0} \\ &\approx \eta_{s0} + 2\alpha_p\left(\frac{-\delta\nu}{\nu}\right)_{sc}(1 - ka \cdot K_1(ka)),\end{aligned} \tag{7}$$

where η_{s0} is the "bare" slip factor without the space charge. As the incoherent space charge tune shift is always negative, the space charge tends to increase the dispersion function and the slip factor. In the isochronous regime, η_{s0} is

zero by definition. Thus, if the machine optics is set to be exactly isochronous, the effective slip factor with the space charge in this case will be

$$\eta_s \approx 2\alpha_p \left(\frac{-\delta\nu}{\nu}\right)_{sc} (1 - ka \cdot K_1(ka)), \qquad (8)$$

In the low energy limit, the compaction factor α_p is equal to unity.

Negative-mass-like instability and its growth rate

The growth rate of the microwave instability is given by the formula [4]

$$\tau^{-1}(k) = \omega_0 \sqrt{-i\frac{\eta_s e I_0 k R_0 Z_{||}}{2\pi\beta^2 E}}, \qquad (9)$$

where ω_0 is the revolution angular frequency, I_0 is the average peak current, and E is the beam full energy.

If $Z_{||}$ is the space charge impedance, the instability can happen only if η_s is positive. In this case, the microwave instability is also referred to as the negative-mass instability. As was shown before, the transverse space charge force effectively increases the dispersion function and the slip factor. Therefore, a negative-mass-like instability can happen even if the machine optics is set below the transition. The growth rate of this instability can be found by inserting (7) into (9). Because the longitudinal space charge impedance peaks at a wave length approximately equal to 2.5 beam diameters, we will use the short wavelength approximation given by (2). If the machine bare optics is exactly isochronous ($\eta_{s0} = 0$), the growth rate is given by

$$\tau^{-1}(k) \approx 2\sqrt{2}\omega_0 \left(\frac{-\delta\nu}{\nu}\right)_{sc} (1 - ka \cdot K_1(ka)) \qquad (10)$$

Thus, the growth rate of this instability at the transition is proportional to the beam current.

If the bare machine optics is set below the transition ($\eta_{s0} < 0$), the instability has a threshold current corresponding to the condition:

$$2\left(\frac{\delta\nu}{\nu}\right)_{sc} \approx \eta_{s0} \qquad (11)$$

In this case, the maximum growth rate depends on the beam current I as

$$\tau_{max}^{-1} \sim I\sqrt{1 - \frac{I_0}{I}} \qquad (12)$$

where I_0 is the threshold corresponding to the condition (11).

SMALL ISOCHRONOUS RING

The Small Isochronous Ring (SIR) is a compact, low energy storage ring designed to simulate the dynamics of intense beams in the isochronous regime. The ring was developed at Michigan State University and has been operational since December 2003.

SIR is designed to run low energy light-ion beams. This choice of beam parameters simplified the ring design and minimized the cost of the project. The ring consists of four 90°, zero-gradient dipole magnets with edge focusing. Figure 3 shows a photograph of SIR. Table 1 gives the main ring parameters. An H_2^+ beam is produced by a multi-cusp ion source, that can be biased up to 30 kV. An analyzing magnet located under the ion source provides charge-to-mass state selection and steers the beam towards the ring. In the injection line, the beam is chopped by a chopper and matched to the ring by a triplet of electrostatic quadrupoles. The bunch length can be changed from 100 nanoseconds ($\sim$15 cm) to 4 microseconds ($\sim$5.5 m). The beam is injected into the ring by a fast pulsed electrostatic inflector. After injection, an injected bunch coasts in the ring. Although the ring does not have RF, the bunch length stays almost unchanged because of the ring isochronism. The beam lifetime in the ring is limited to approximately 200 turns due to electron pickup from the residual gas. After a chosen number of turns, the bunch is deflected towards either a phosphor screen or a Fast Faraday Cup (FFC) situated above and below the median plane respectively. The Faraday Cup measures the longitudinal beam profile of the beam with a time resolution of 1 ns corresponding to a spatial resolution of approximately 1-1.5 mm. The phosphor screen is used to observe the transverse beam profile. Changing the extraction turn number, we can observe temporal evolution of the longitudinal and radial beam profiles in the ring.

Figure 3: Small Isochronous Ring

Table 1: Primary SIR parameters.

Beams	H_2^+
Energy	10-30 keV
ν_x, ν_y	1.14, 1.11
α_p-1/γ^2	$1.7 \cdot 10^{-4}$
C	6.6 m
Rev. period	5 μsec
$N_{\rm turns}$, up to	200
$I_{\rm peak}$, typical	0-25 μA

SIMULATIONS OF BEAM DYNAMICS IN SIR

The code CYCO [1] was used to simulate the beam dynamics in SIR. The code calculates particle trajectories in a realistic 3D magnetic field map, solving the full, unsimplified system of equations of motion with the space charge. The code uses the classical 4^{th} order Runge-Kutta integration method to numerically solve the system. The space charge field of the beam is calculated by a PIC field solver. The solver employs Fast Fourier Transforms and the fast convolution theorem to calculate the beam field. In calculating the space charge field, the program includes the effect of image charges induced on the vacuum chamber assuming that the vacuum chamber consists of two parallel perfectly conducting planes. No other impedance besides the space charge is included.

The initial beam distribution was chosen to mimic the phase space of the real beam measured by pairs of moving slits and a fast faraday cup. The transverse distribution was a uniform 4D distribution

$$f = H\left(1 - \frac{A_x}{\epsilon_x} + \frac{A_y}{\epsilon_y}\right), \qquad (13)$$

where H is the Heaviside function. A_x and A_y are Courant-Snyder invariants in the horizontal and vertical planes. The maximum values of Courant-Snyder invariants in x and y were the same, $\epsilon_{x,y} = 5 \cdot 10^{-5}$ m, corresponding the beam diameter in the ring approximately equal to 1 cm. The initial longitudinal distribution was uniform. For most of our simulations, we used a 40 cm long bunch with hard edges. The initial energy spread was zero. According to the operational experience with multi-cusp ions sources, sources of this type typically produce an energy spread of a few eV's, yielding a relative energy spread of $\sim 10^{-4}$. Because of its small value, the initial energy spread was completely neglected in the simulations.

Beam instability/fragmentation

Simulations of the beam dynamics in SIR show that the space charge force causes fast beam fragmentation. This break-up is accompanied by a fast growth of the energy spread. Figure 4 shows formation of droplet-like clusters for three different beam intensities. The machine optics was set in the isochronous regime in these simulations.

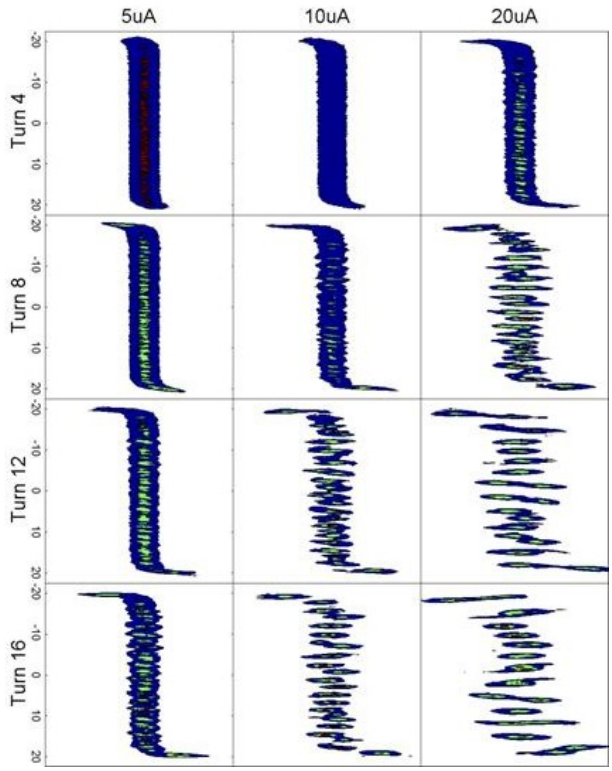

Figure 4: Beam breakup for three different peak intensities: 5, 10, and 20 μA. The "bare" machine optics is isochronous. Each frame contains a projection of the bunch charge density on the median plane for a given turn and intensity. The velocity of bunches is directed from the top of the figure to the bottom. The horizontal side of each frame corresponds to x while the vertical side is along the bunch length. The size of each frame is 5×40 cm.

Fig. 5 shows evolution of the linear particle density in the central part of the bunch for a peak current of 10 μA. The linear charge density is shown for turns 7, 11, and 15. Fig. 6 shows the FFT spectrum of the profiles shown in Fig. 5.

Fig. 7 shows the logarithm of the amplitude of five different harmonics as a function of the turn number. All the curves with an only exception of the harmonic with the wavelength $\lambda = 3$ cm show an exponential growth starting from turn 1 up to turn 11 or 12. After turn 12, the growth saturates. The harmonic with $\lambda = 1.5$ cm exhibits the highest growth rate. The curve corresponding to $\lambda = 3$ cm starts growing after turn 5 and does not exhibit saturation below turn 15. Fig. 8 shows the growth rate for the mentioned above harmonics. Also, Fig. 8 shows the growth rate for four different peak intensities: 5, 10, 15 and 20 μA.

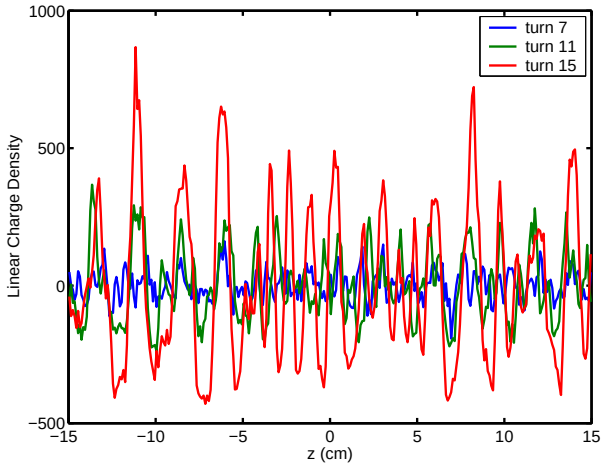

Figure 5: Linear particle density profiles for turns 7, 11, and 15. The peak beam current was 10 μA. The average level was subtracted. Only the central $\pm$15 cm part of a 40 cm long bunch is shown. The charge density is in arbitrary units.

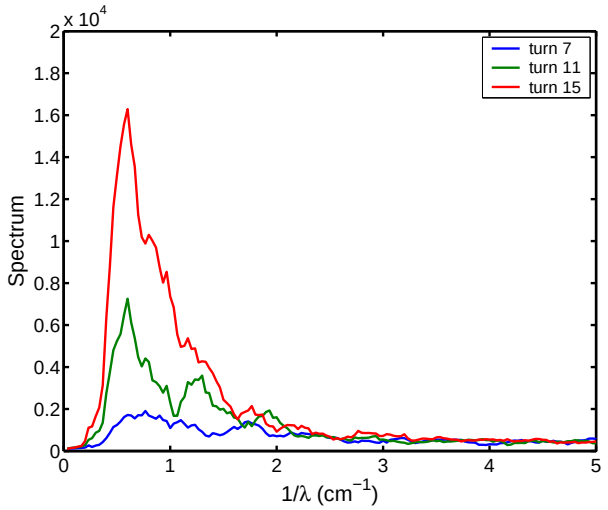

Figure 6: Spectrum of linear charge density for turns 7, 11, and 15 shown in Fig. 5.

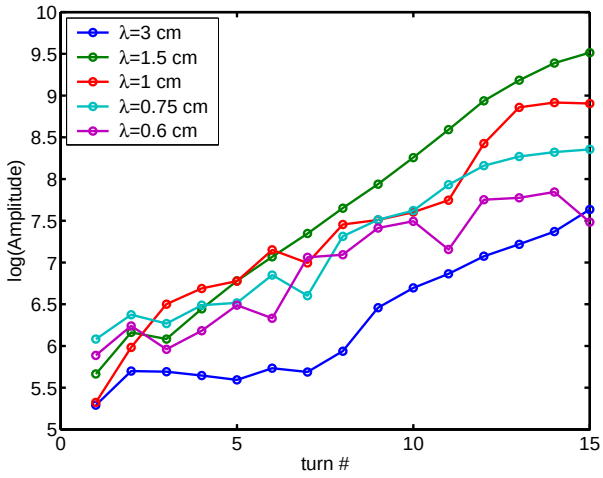

Figure 7: Logarithm of the amplitude of harmonics with λ=0.6, 0.75, 1, 1.5, and 3 cm as a function of the turn number. The harmonic with $\lambda = 1.5$ cm exhibits the highest growth rate.

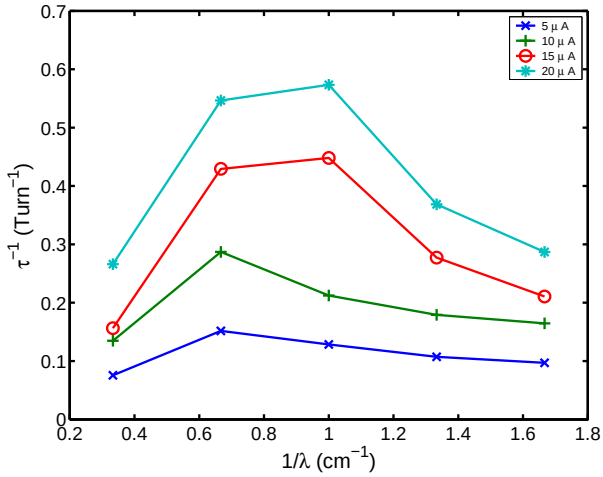

Figure 8: Amplitude growth rate for harmonics with the wavelength λ=0.6, 0.75, 1, 1.5, and 3 cm. The growth rate shown for four different peak intensities: 5, 10, 15 and 20 μA.

Scaling with the beam current

First, we simulated the beam dynamics in the isochronous SIR optics. The slip factor in the SIR model was $+2 \cdot 10^{-4}$. It was adjusted specifically to match the measured SIR slip factor. Fig. 9 shows the growth rate for four different peak intensities: 5, 10, 15 and 20 μA, similar to those shown in Fig. 8 but normalized on the beam current. The normalized curves practically overlap in the region λ=1.5 cm and are close to each other in other regions. Thus, Fig. 9 demonstrates that the growth rate of the instability scales practically linearly with the beam current. This is expected if the effect of the transverse space charge force is included (see Eq. 10). In the case of the classical negative mass instability, when only the longitudinal SC field is included, the growth rate should be proportional to the square root of the peak current, which contradicts the simulations and experimental data described below. Also note that that observed growth rate significantly exceeds the growth rate, which would result from the constant slip factor $+2 \cdot 10^{-4}$. Table 2 shows the maximum negative mass instability growth rate calculated using the constant slip factor $\eta_{s0} = 2 \cdot 10^{-4}$.

To simulate the beam dynamics below the transition the distance between SIR dipole magnets was increased by 9 cm that yielded a slip factor of -0.04. In this optics, the beam with a peak current of 5 μA exhibited no instability behavior all the way up to the maximum number of simulated turns (100). The other three simulated cases with

Table 2: Amplitude growth rate of the harmonic λ=1.5 cm observed in simulations and calculated assuming the constant slip factor $\eta_{s0} = +2 \cdot 10^{-4}$

I_0 (μA)	τ^{-1} (Turn^{-1}) With SC	τ^{-1} (Turn^{-1}) No SC $\eta_s = +2 \cdot 10^{-4}$
5	0.15	0.02
10	0.29	0.028
15	0.43	0.034
20	0.55	0.038

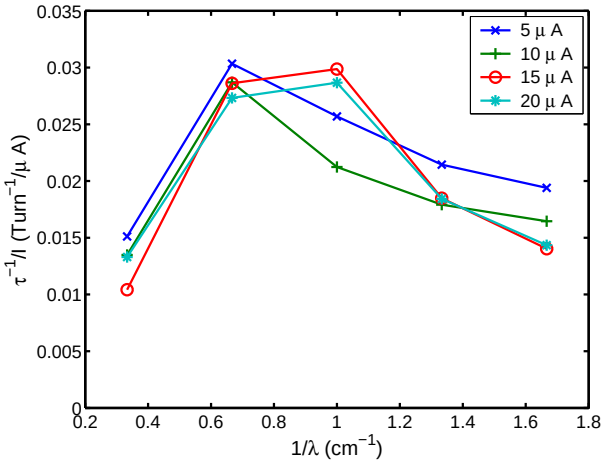

Figure 9: Amplitude growth rate for harmonics with the wavelength λ=0.6, 0.75, 1, 1.5, and 3 cm normalized on the peak beam current. The normalized growth rate shown for four different peak intensities: 5, 10, 15 and 20 μA.

the beam peak current equal to 10, 15 and 20 μA exhibited the instability and clustering. Fig. 10 shows the amplitude growth rate of the harmonic with λ=1.5 cm as a function of the beam current for the optics with the negative slip factor and the fit $y = 0.028x\sqrt{1-7/x}$. Also, Fig. 10 shows the amplitude growth rate for the isochronous case and the linear fit $y = 0.028x$. The good agreement between the simulated growth rates and the fits confirms that the formulae presented above correctly predict the dependence on the beam current, indicating the correctness of the proposed physical model. Additionally, Fig. 10 shows the growth rates directly calculated from (10) and (12). The incoherent space charge tune shift used to calculate theoretical growth rates was estimated numerically from the fit $y = 0.028x\sqrt{1-7/x}$ and Eq. (11). According to Fig. 10, equations (10) and (12) predict growth rates approximately 60% higher than those observed.

EXPERIMENTAL STUDIES OF BEAM DYNAMICS IN SIR

In this section, we present results obtained in experiments conducted at MSU in 2003-2004. The experimental

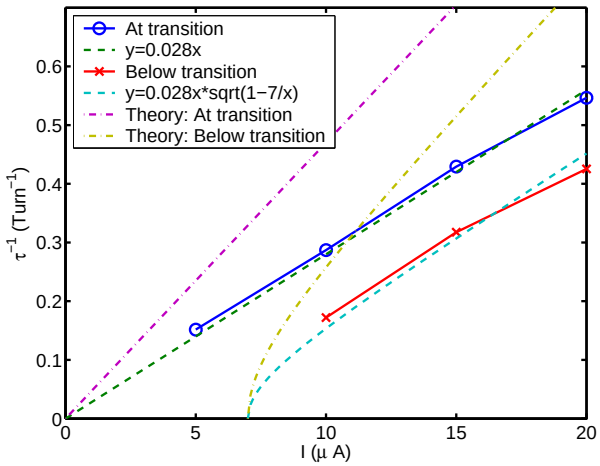

Figure 10: Growth rate of the harmonic with λ=1.5 cm for the isochronous optics and the optics with the negative slip factor -0.04. The simulated data is fitted with corresponding fits: $y = 0.028x$ and $y = 0.028x\sqrt{1-7/x}$. Additionally, growth rates calculated directly from Eq. (10) and (12) are shown.

studies of the beam dynamics in SIR were conducted in the isochronous regime. The SIR slip factor η_{s0} was set to almost zero and measured by the time of flight technique that yielded $\eta_{s0} = +1.7 \cdot 10^{-4}$.

To quantify experimental results we counted the number of peaks of the longitudinal charge density, sometimes referred to as clusters. The density peaks were defined relatively to a chosen level of the initial charge density. This observable provided us with the following information: a) when modulation of the longitudinal charge density reached a given level and b) what was the size of charge density peaks. Unfortunately, this observable gave us only limited amount information omitting many details. Observing evolution of the beam spectrum, for example, could give us better insight into the beam dynamics. However, this paper presents the original experimental results unchanged.

Comparison of simulation results and experimental data

Fig. 11 shows the simulated and measured number of linear charge density peaks as a function of turn number. The threshold at which density perturbations were counted was set to 50% of the initial density level. In the figure, simulation and experimental results were overlaid on top of each other for three different beam intensities. The simulation data shows an average number of peaks corresponding to 14 different randomly seeded distributions. The width of the curves corresponds to two standard deviations of the number of peaks. The experimental data shows the result of processing of 100 distributions for each turn. According to the figure, the simulation results agree remarkably well with the experimental data.

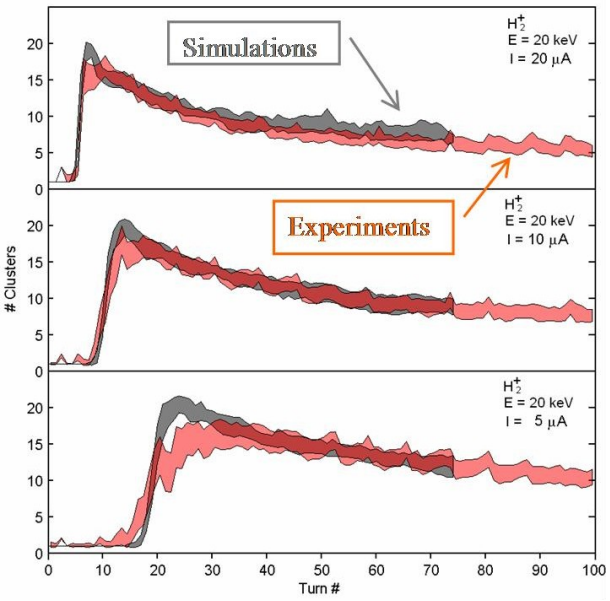

Figure 11: Simulated and experimentally measured number of linear charge density peaks vs. turn number. Experimental and measured data closely overlap.

Scaling with the beam current

Figure 12 shows the measured number of peaks as a function of turn number for three different beam intensities. The data is shown as a function of the product of turn number and beam intensity. The overlap of the curves corresponding to different beam intensities confirms linear dependence of the instability growth rate on the beam current.

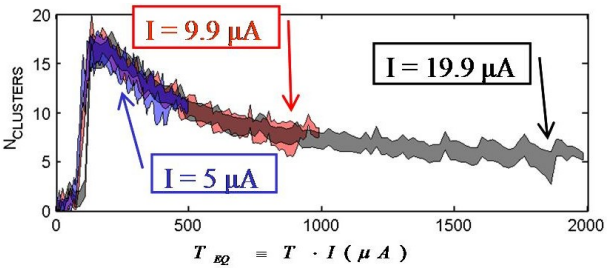

Figure 12: The number of peaks of the linear charge density as a function of the product of turn number and beam intensity shown for three different peak intensities: 5, 10, and 20 μA.

Scaling with the bunch length

Figure 13 shows evolution of the measured number of peaks for three different bunch lengths. If the number of peaks is divided by the initial bunch length, all the three curves practically overlap. This indicates that the instability happens throughout a bunch that contradicts our original expectation that clustering should have slowly propagated from the ends inside the bunch. This result also shows that the size of clusters that form as a result of the instability does not depend on the bunch length.

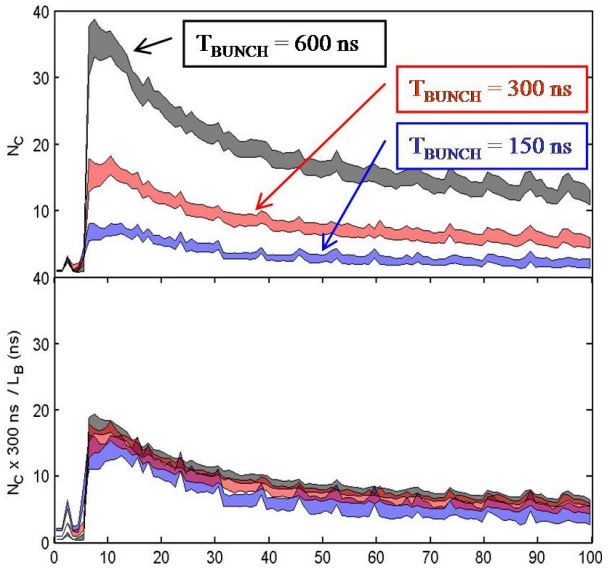

Figure 13: The number of peaks of the linear charge density for three different bunch lengths: 20, 40, and 80 cm. The breakup almost does not depend on the bunch length.

CONCLUSIONS

The proposed model of the space charge driven instability explains the observed and simulated beam behavior in SIR at and below the isochronous regime with a reasonable accuracy, especially considering the simplistic nature of the analysis presented in the paper. The described model has to be extended to include relativistic effects in order to predict the effect of the instability in large scale, high energy machines. Additionally, the Landau damping caused by the incoherent energy spread has to be included in the model.

ACKNOWLEDGEMENTS

We would like to thank D. Deveraux, R. Fontus, D. Sanderson, A. Zeller and R. Zink for extensive help during the design and construction of SIR. We would also like to thank the personnel of the NSCL shop for their work in machining several of the SIR components, including the dipole magnets. We would also like to thank Lawrence Berkeley National Laboratory for lending us the multi-cusp source used in SIR.

REFERENCES

[1] E. Pozdeyev, "CYCO and SIR: New Tools for Numerical and Experimental Studies of Space Charge Effects in the Isochronous Regime", Thesis, MSU, 2003.

[2] J.A. Rodriguez, "Studies of Longitudinal Beam Dynamics With Strong Space Charge Effects Using a Small Isochronous Ring", Thesis, MSU, 2004.

[3] S.A. Bogacz, Proceedings of 2^{nd} EPAC, (Nice, France, 1990), p. 1524

[4] K.Y. Ng, "Physics of Intensity Dependent Instabilities" US-PAS Lecture Notes, Los Angeles (January 2002), FNAL Report Fermilab-FN-0713

[5] A.W. Chao, M. Tigner, "Handbook of Accelerator Physics and Engineering", World Scientific Publishing Company (March 26, 1999)

[6] S. Adam, Proceedings of 14^{th} Int. Cycl. Conf. (Cape Town, 1995), p.446, World Scientific, Singapore.